Regulating the Phase and Optical Properties of Mixed-Halide Perovskites via Hot-Electron Engineering

Chun-Ho Lin, Changxu Liu,* Jialin Yang, Jiyun Kim, Long Hu, Chien-Yu Huang, Shuo Zhang, Fandi Chen, Rishabh Mishra, Shamim Shahrokhi, Jing-Kai Huang, Xinwei Guan, Alexander J. Baldacchino, Tao Wan, Shujuan Huang, Michael P. Nielsen, Kewei Liu, Dewei Chu,* Stefan A. Maier, and Tom Wu*

The rapid development of mixed-halide perovskites has established a versatile optoelectronic platform owing to their extraordinary physical properties, but there remain challenges toward achieving highly reliable synthesis and performance, in addition, post-synthesis approaches for tuning their photoluminescence properties after device fabrication remain limited. In this work, an effective approach is reported to leveraging hot electrons generated from plasmonic nanostructures to regulate the optical properties of perovskites. A plasmonic metasurface composed of Au nanoparticles can effectively tailor both photoluminescence and location-specific phase segregation of mixed-halide $CsPbI_2Br$ thin films. The ultrafast transient absorption spectroscopy measurements reveal hot electron injection on the timescale of hundreds of femtoseconds. Photocurrent measurements confirm the hot-electron-enhanced photon-carrier conversion, and in addition, gate-voltage tuning of phase segregation is observed because of correlated carrier injection and halide migration in the perovskite films. Finally, the characteristics of the gate-modulated light emission are found to conform to a rectified linear unit function, serving as nonlinear electrical-to-optical converters in artificial neural networks. Overall, the hot electron engineering approach demonstrated in this work provides effective location-specific control of the phase and optical properties of halide perovskites, underscoring the potential of plasmonic metasurfaces for advancing perovskite technologies.

1. Introduction

Halide perovskites have emerged as a class of highly sought-after materials for various optoelectronic applications, including solar cells, light-emitting diodes, photodetectors, and lasing devices.[1–6] Perovskite solar cells have been extensively exploited in the past decade and realized a single-junction efficiency exceeding 26%, making them the fastest-advancing photovoltaic materials so far.[7] The superior optoelectronic characteristics, such as high absorption coefficient, excellent carrier mobility and lifetime, defect-tolerant nature, and direct bandgap, make perovskite materials desirable for conducting efficient photoelectric conversion.[8–11] Furthermore, the versatility of the perovskite structure $APbX_3$ (A = MA, FA, and Cs; X = Cl, Br, and I) allows ionic mixing on the A- or X-site, which provides ample opportunities to modify the optoelectronic properties of perovskites.[12] Particularly, halide ratio engineering is the prevalent technique for tuning the optical bandgap of mixed-halide perovskite to cover the whole visible light spectrum from 380 nm to 760 nm, thus meeting the demands of a wide range of applications.[2,13]

C.-H. Lin, J. Kim, L. Hu, C.-Y. Huang, S. Zhang, F. Chen, S. Shahrokhi, J.-K. Huang, X. Guan, T. Wan, D. Chu, T. Wu
School of Materials Science and Engineering
University of New South Wales (UNSW)
Sydney, NSW 2052, Australia
E-mail: d.chu@unsw.edu.au; tom.wu@unsw.edu.au

C. Liu
Centre for Metamaterial Research & Innovation, Department of Engineering
University of Exeter
Exeter EX4 4QF, UK
E-mail: c.c.liu@exeter.ac.uk

J. Yang, K. Liu
State Key Laboratory of Luminescence and Applications (SKLLA), Changchun Institute of Optics, Fine Mechanics, and Physics (CIOMP)
Chinese Academy of Science (CAS)
Changchun 130033, China

L. Hu, S. Huang
School of Engineering
Macquarie University
Sydney, NSW 2109, Australia

**ADVANCED
SCIENCE NEWS**

www.advancedsciencenews.com

**ADVANCED
FUNCTIONAL
MATERIALS**

www.afm-journal.de

Further modulation of the perovskite properties may be achieved with hot carriers which have been envisioned to enable novel applications, including photovoltaics, photocatalysis, and photodetectors, via circumventing bandgap limitations.[14–16] Through strong light-matter interactions, hot electrons are endowed with energy much higher than the ones at thermal equilibrium, thereby potentially facilitating a wide range of thermodynamic processes.[17–19] Metasurfaces made from metal nanoparticles (NPs) with subwavelength dimensions have demonstrated extraordinary capability to produce localized resonances and to couple hot electrons into semiconductors.[20–23] In a recent work, Huang et al. investigated the interface between metal NPs and perovskite and discovered a markedly high hot-electron transfer efficiency,[20] suggesting a strong coupling effect. However, the deliberate control of perovskite properties through hot-electron engineering remains a nascent field that is yet to be extensively explored. Furthermore, injecting hot carriers into perovskites represents a highly sought-after strategy for post-synthesis modulation of the physical properties and achievement of reliable device operation.

In the prevalently employed mixed-halide perovskites, it is well recognized that under even mild external stimuli, phase segregation often occurs and modifies the characteristics of perovskites.[24–29] For example, under light irradiation, the change of thermodynamic free energies can lead to the destabilization of mixed-halide states.[30–31] Up to date, significant efforts have been made to investigate and tune the phase segregation in mixed-halide perovskites.[32–35] In a representative work, Gualdron-Reyes et al. demonstrated the control of phase segregation through nanocrystal size tuning, and they found that phase separation becomes severe when the nanocrystal size exceeds the charge diffusion length.[34] Recently, our group also employed the thermal annealing technique to control the grain size and phase segregation in mixed-halide perovskite thin films for achieving reliable solar cells.[35] The primary focus of current research efforts is on material engineering aimed at mitigating phase segregation and enhancing the stability of perovskites. Meanwhile, there are some reports on unexpected observations showing that phase segregation could be a double-edged sword in regulating physical properties. For example, Caprioglio and coworkers recently demonstrated the enhanced radiative efficiency and quantum yield of the phase-segregated perovskites,[36] and Motti et al. observed the increased charge-carrier mobility in segregated I-rich domains using Terahertz spectroscopy.[37] These phenomena underscore the complexity of phase segregation that necessitates further research. In this context, the capacity to manipulate phase segregation is crucial for advancing our understanding and potentially unveiling novel applications. However, despite all the efforts, few strategies are available to control phase segregation in mixed-halide perovskite films.

Considering the potential of hot-electron engineering, we postulate that hot carriers from plasmonic nanostructures can be leveraged as an external stimulus to modulate the phase segregation in mixed-halide perovskites. Despite remaining uncharted territory, imposing plasmonic metasurfaces on mixed-halide perovskites provides a valuable opportunity to control the phase and properties via leveraging the light-matter interactions and hot-electron coupling. This study demonstrates such an approach of hot electron engineering to regulate the phase segregation and optical properties of mixed-halide perovskite $CsPbI_2Br$ (CPIB). A significantly enhanced photoluminescence (PL) and phase segregation of the mixed-halide perovskite films were observed when a plasmonic metasurface was introduced atop, suggesting the effective role of hot carriers, which was confirmed by a complementary suite of PL, absorption spectroscopy, and current-voltage (I-V) measurements as well as simulation results. Furthermore, we found that the hot-electron transfer and associated phase segregation can be tuned by a gate bias, which provides an additional tool to actively regulate the optoelectronic properties of mixed-halide perovskites. As a proof-of-concept, we demonstrated that the gate voltage input and iodine-domain light output of the perovskite device follows a rectified linear unit (ReLU) function, thus suggesting the potential of metasurface/perovskite heterostructures as nonlinear electrical-to-optical converters in artificial neural networks.

2. Results and Discussion

As illustrated in **Figure 1**a, a plasmonic metasurface composed of high-density hemisphere-like Au NPs was designed and fabricated on top of the mixed-halide perovskite layer. Among the variables of experimental configuration, such as the dimensions of Au NPs and the incident light wavelength, the perovskite layer thickness plays a vital role in the light-matter interactions. According to recent reports, the thickness of the semiconductor, or equivalently the resonance of the Fabry–Pérot cavity, can impact the absorption of the plasmonic metasurface above.[38] Meanwhile, the top metasurface can act as an auxiliary layer to enhance the absorption of the semiconductor beneath by maximizing the near-field. On the other hand, certain designs may result in absorption loss due to the thickness mismatch and shading effect from metal NPs.[39] This flexibility of the thickness selection can drive the device to operate in a regime where the additional hot-electron generations enhance the photo-carriers produced in the perovskite layer, consequently tuning or even improving the device performance. To search for the target thickness, we performed a simulation of optical absorption for the perovskite layers with different layer thicknesses coupling with Au NP

R. Mishra, A. J. Baldacchino, M. P. Nielsen
School of Photovoltaics and Renewable Energy Engineering
UNSW
Sydney, NSW 2052, Australia

X. Guan
School of Science
RMIT University
Melbourne, VIC 3000, Australia

S. A. Maier
School of Physics and Astronomy
Monash University
Clayton, VIC 3800, Australia

S. A. Maier
Department of Physics
Imperial College London
London SW7 2AZ, UK

T. Wu
Department of Applied Physics
The Hong Kong Polytechnic University
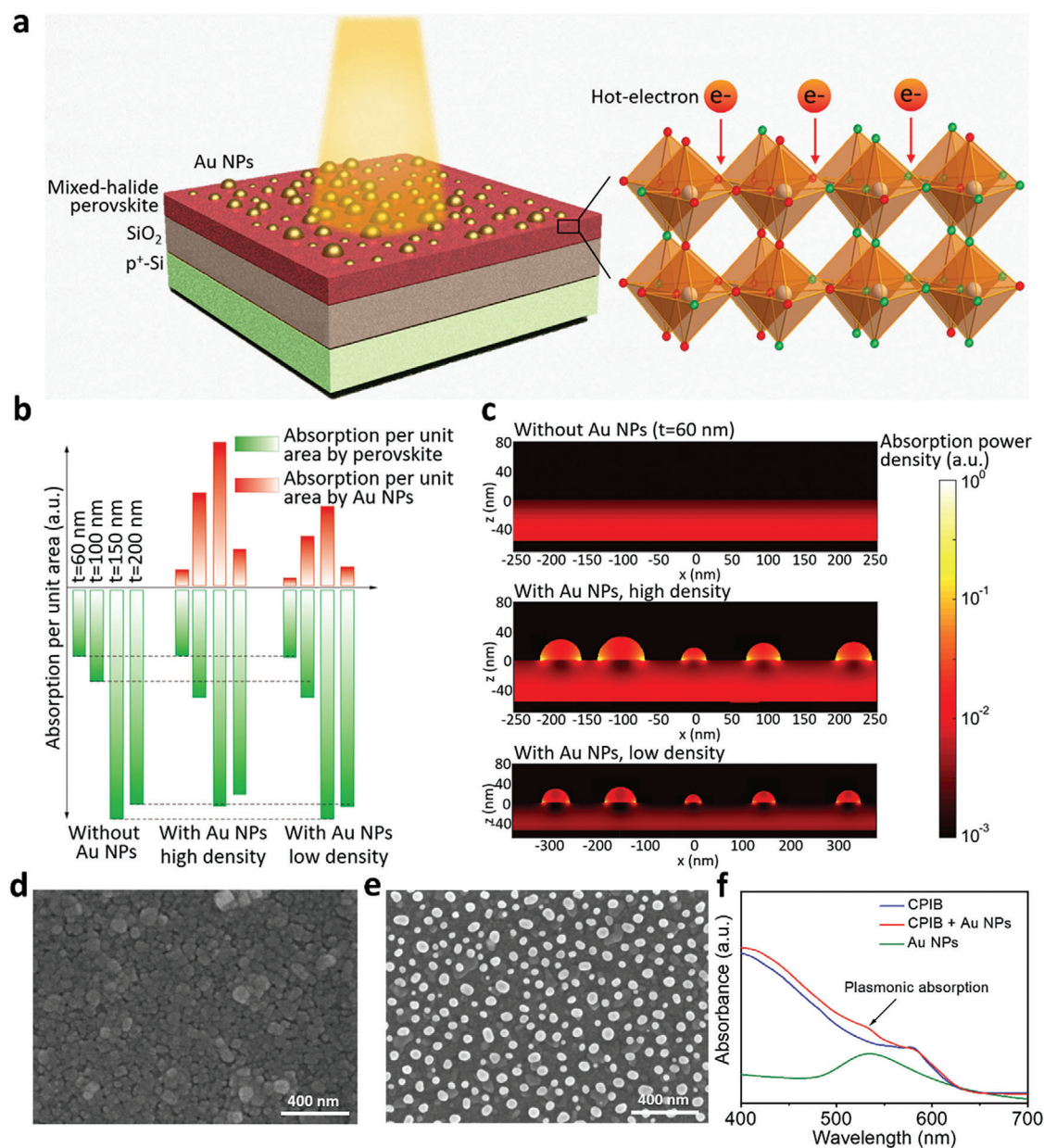Kowloon, Hong Kong 999077, China

Figure 1. a) Illustration of the Au NP metasurface on the mixed-halide perovskite thin film and hot-electron injection. b) Simulated optical absorption of CPIB layers (thickness: 60, 100, 150, and 200 nm) without and with Au NPs (high density: one NP per 100 nm × 100 nm; low density: one NP per 150 nm × 150 nm) under 532-nm light illumination. c) Simulated distribution of absorption power density in 60-nm-thick CPIB layers without and with Au NPs under 532-nm illumination. Top-view SEM images of d) pristine CPIB film and e) CPIB film with Au NP metasurface structures. f) UV–vis absorption spectra of pristine CPIB film, Au NPs/CPIB hybrid film, and pure Au NPs.

metasurface structures (Figure 1b). Among the thicknesses considered, a desirable thickness of 60 nm was identified as the most suitable one, with which the absorption power per unit area of perovskite remains nearly unchanged after introducing a high-density Au NP metasurface structure, as shown in Figure 1c. This design helps exclude the influence of optical variation so that the impact of hot-electron injection on perovskite can be exclusively investigated. In contrast, the thicker perovskite films may lead to certain degrees of change in perovskite absorption (Figure 1b).

To effectively couple with Au NPs with high oscillation strength,[40] we employed perovskite thin films based on nanocrystals with controlled thicknesses and good surface coverage.[41] Since small-sized inorganic perovskite nanocrystals have high oscillation strength,[20] they have a good match with the plasmonic metasurface to enable efficient hot-electron transfer. The characterizations of synthesized CPIB perovskite nanocrystals can be found in Figure S1 (Supporting Information), and thin perovskite films of ≈60 nm were prepared by the spin-coating method (see Supporting Discussion and Figures

ADVANCED
SCIENCE NEWS

www.advancedsciencenews.com

ADVANCED
FUNCTIONAL
MATERIALS

www.afm-journal.de

S2–S5 in the Supporting Information). To fabricate the plasmonic metasurfaces, half of the perovskite films were deposited with 11.4 μg cm^{-2} Au utilizing thermal evaporation, and then, after rapid annealing, the NP nanostructures were generated. The film was examined using a scanning electron microscope (SEM), as displayed in Figure 1d,e, and Figure S3 (Supporting Information), showing well-constructed perovskite thin film and hemisphere-shaped Au NP metasurface structures.

To further examine the optical absorption of CPIB films and Au NP structures, UV–vis spectroscopy measurements were carried out. As shown in Figure 1f, the pristine CPIB film exhibits a band edge cut-off at around 635 nm that corresponds to a Tauc optical bandgap of 1.95 eV (Figure S6, Supporting Information). For the Au NPs/CPIB hybrid film, an additional absorption peak at 535 nm that corresponds to the local mode of surface plasmon resonance of Au NPs was observed, indicating enhanced plasmonic absorption in the metasurface/perovskite structures. Note that the absorption baselines of perovskites with and without Au NPs are well-matched (in wavelength region >570 nm), which is consistent with our simulation result that the perovskite optical absorption remains unchanged.

The presence of plasmonic Au NPs exerts a significant influence on the photoluminescence properties of the mixed-halide perovskite films because of strong Au NP resonance, revealed by the simulation results (**Figure 2a**; Figure S7, Supporting Information). Figure 2b shows the steady-state PL spectra of both pristine CPIB and Au NPs/CPIB films excited by a 532-nm laser, which matches well with the plasmonic peak of Au NPs at 535 nm. With Au NPs on the surface, a notable increase in the PL intensity was obtained. PL mapping on the CPIB film over the boundary between the regions with and without Au NPs is shown in the inset of Figure 2b. An overall enhancement of the PL intensity was observed in the region covered with the Au NP metasurface, in good agreement with the steady-state PL results. In general, the incident light may produce several effects in the Au NPs/CPIB, including far-field light scattering, near-field plasmonic resonance, and hot electron transfer.[42,43] Herein, even though the Au NPs might cause some light scattering, this is not the source of enhanced PL as the scattered photons might not be collected by the spectroscopy setup (without an integrating sphere), and any light scattering effect would decrease the PL of the film. On the other hand, the near-field resonance between plasmonic NPs and incident photons produces localized electromagnetic field enhancement and resonant oscillation of conduction electrons, and the resultant increase in spontaneous emission rate is known as the Purcell effect.[42] Thus, the significantly enhanced PL observed in Au NPs/CPIB is consistent with the existence of the Purcell effect due to strong intensity at the near-field. On the other hand, hot-carrier injection also plays an important role since it can enhance the population of excitons and make a profound impact on the optical properties of the perovskite,[44] which will be discussed in a later section. The notably enhanced PL intensity observed here also suggested that the regulation of the optical property of the perovskite films is induced by the plasmonic metasurfaces rather than the potential defects due to Au NPs/CPIB reaction or Au diffusion because such defects would quench the PL through nonradiative recombination. To explore the universality of the metasurface-based approach to enhancing the PL of perovskite films, another supplementary experiment was performed

on a CsPbBr$_3$ film, and significantly enhanced PL emission was also observed (Figure S8, Supporting Information).

To understand the PL characteristics in-depth, time-resolved PL measurements were also performed on the perovskite films, as shown in Figure S9 (Supporting Information). The PL decay curves were analyzed using the biexponential fitting, in which the short carrier lifetime τ_1 (surface recombination) and long carrier lifetime τ_2 (bulk recombination) are 3.3 ns and 17.1 ns for the pristine CPIB and 2.3 ns and 9.6 ns for the Au NPs/CPIB, respectively. The shortened PL decay of Au NPs/CPIB can be attributed to the perovskite/metasurface heterostructure interface that actuates fast charge transfer from CPIB to Au NPs and reduces carrier recombination.[45] Similar observations of reduced PL lifetimes have also been reported in other plasmon/semiconductor systems due to interfacial charge transfer.[46–48] Here, the charge transfer in the time-resolved PL measurement could be complex as mixed-phase perovskite, Br/I-rich regions, and Au NPs all exist in the system. Also, it is worth mentioning that interfacial defects might also reduce the PL lifetime, and thus the synergistic effect of charge transfer and interfacial recombination leads to the fast decay of PL at the Au NPs/CPIB interface.

We then measured the PL spectra of the pristine CPIB under continuous excitation with a 532-nm laser at an intensity of 5 mW cm^{-2} (Figure 2c). A redshift of the PL peak from 629 nm to 690 nm was observed after 15 min illumination, suggesting the onset of I-rich emission and phase segregation because of light-induced halide diffusion. In comparison, as shown in Figure 2d, the PL shift in the Au NPs decorated CPIB was much faster under the same illumination condition and took only 4 min, indicating that the plasmonic metasurface can significantly promote and accelerate the halide segregation in the mixed-halide perovskite film.

Localized surface plasmon resonance and hot-electron transfer are crucial coupling routes in hot-electron optoelectronics, as illustrated in Figure 2e. Upon light excitation, the localized surface plasmon resonance or so-called Landau damping tends to generate hot carriers with higher energy than typical photoexcited carriers, which can more easily transfer across the Schottky interface and couple with the conduction electrons in the perovskite.[15] From the energetic point of view, thermodynamic variation of the Gibbs free energy plays a critical role in dictating the light-induced phase segregation in mixed-halide perovskites.[27,30,33,49] Upon light illumination, the absorbed photon energy can generate high-density photocarriers, which increases the overall Gibbs free energy in the system and enhances the phase segregation.[49] With the additional metasurface imposed as in our study, the strong localized plasmon resonance causes the injection of high-energy hot electrons into the CPIB film. Consequently, the equivalent carrier concentration in CPIB is effectively enhanced under continuous light illumination as evidenced by the enhanced steady-state PL (Figure 2b), thereby accelerating the phase segregation behavior.

It is worth noting that the phase segregation phenomena in both the pristine and the Au NPs/CPIB films are reversible in dark. As shown in Figure 2f and g, the PL spectra of phase-segregated samples almost returned to their original mixed-halide states after storage in dark for 50 min. Additionally, photoinduced halide segregation and dark recovery of Au NPs/CPIB were repeated 10 times, indicating a fully reversible process
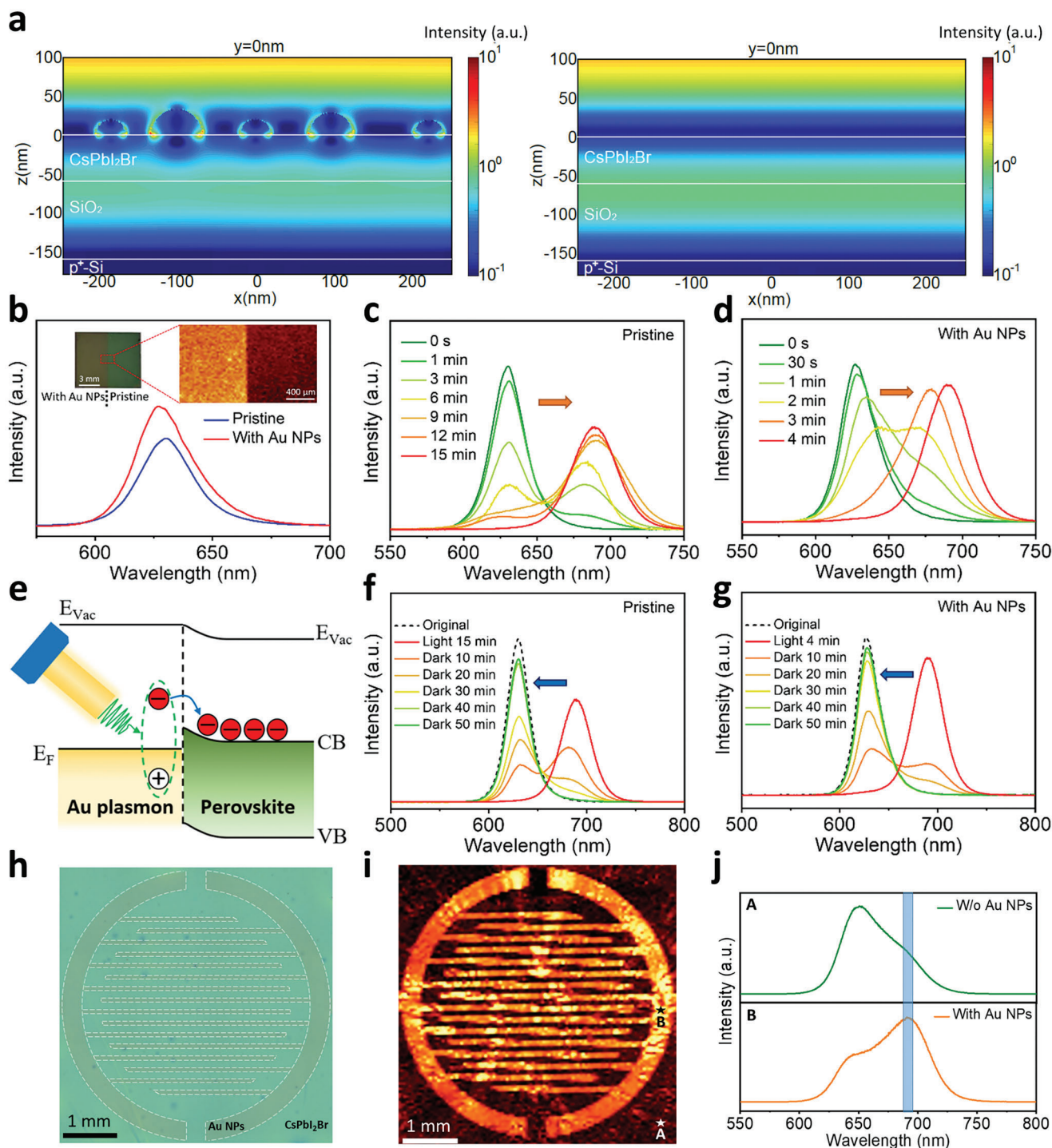
Figure 2. a) Simulation of cross-sectional field distribution of CPIB/SiO$_2$/Si with and without Au NPs at the wavelength of 532 nm, showing a strong resonance of the Au NP metasurface. b) Steady-state PL spectra of the pristine CPIB film and the Au NPs/CPIB hybrid structure. The inset demonstrates the PL mapping result over the two perovskite regions with and without the plasmonic Au NP structure. PL evolution of c) the pristine CPIB film and d) the Au NPs/CPIB film under the continuous illumination of a 532-nm laser (5 mW cm^{-2}). e) Illustration of localized surface plasmon resonance and hot-electron transfer from the Au plasmon to the perovskite film. PL evolution of f) the pristine CPIB film and g) the Au NPs/CPIB film during dark recovery. h) Optical microscope image of the Au NPs patterned CPIB film. The Au patterned regions are marked by white dashed lines. i) PL mapping of the Au NPs/CPIB film with a filter wavelength of 690 nm (I-rich emission). j) PL spectra obtained from the positions A (without Au NPs) and B (with Au NPs) marked in Figure 2i. The filter wavelength employed for PL mapping is highlighted.

ADVANCED
SCIENCE NEWS

www.advancedsciencenews.com

ADVANCED
FUNCTIONAL
MATERIALS

www.afm-journal.de

(Figure S10, Supporting Information). When the light illumination on the sample was turned off, the free carrier concentration in CPIB film was reduced and the overall Gibbs energy changed,[49] which led to the remixing of segregated halide ions.[50]

The metasurface-dependent characteristics discussed above suggest the effectiveness of hot electron management in fine-tuning the phase segregation and photoluminescence property of mixed-halide perovskite films. In addition, unlike previously reported approaches of crystal size engineering or thermal annealing that tunes the phase segregation property of entire perovskite specimens,[34,35] the metasurface nanostructures allow specific control of halide phase and photoluminescence in localized positions owing to the near-field nature of plasmonic metasurface. As a proof of concept, we selectively patterned the metasurface on a CPIB film and studied its PL characteristics. The experimental procedures are illustrated in Figure S11 (Supporting Information). First, the Au NPs were patterned on CPIB film through a shadow mask with a circular intercrossing structure as shown in the optical microscope image in Figure 2h. Then, the patterned Au NPs/CPIB film was illuminated by solar simulator AM 1.5G for 1 min to induce phase segregation. Note that the resonant wavelength region of Au NPs (from 500 nm to 600 nm) matches the intense radiation region of AM 1.5G (Figure S12, Supporting Information), and therefore, the Au NPs can efficiently generate hot carriers and inject them into semiconductor systems as reported in the literature.[51,52] After light illumination, PL mapping was executed on the perovskite film and the filter wavelength was set to 690 nm, which corresponds to the I-rich emission. The mapping result in Figure 2i displays an obvious boundary, and the bright yellow color in the Au plasma patterned region indicates the significant enhancement of iodine emission. The PL spectra of CPIB film without (point A) and with Au NPs (point B) are taken and shown in Figure 2j. The enhanced I-rich emission can be seen for point B, signifying that the metasurface structures can regulate the photoluminescence and phase segregation at localized positions.

While it is generally believed that phase segregation should be avoided for achieving reliable device performance, recent studies unveiled the enhanced properties in terms of radiative efficiency, quantum yield, carrier mobility, and carrier lifetime at phase-segregated I-rich domains.[36,37,50] The metasurface-enabled location-specific regulation of the phase segregation phenomenon presents a new opportunity to innovate the device design and to advance the performance of optoelectronic devices based on mixed-halide perovskites.

To further investigate the dynamics of hot electron injection, ultrafast transient absorption spectroscopy (TAS) was used in this study. Three effects may occur when a light pulse incident to the Au NPs/CPIB structure, including (i) photocarrier excitation, (ii) hot-electron transfer, and (iii) phase segregation. Hot-electron transfer typically features a longer time scale than photocarrier excitation and can be distinguished in a TAS spectrum. However, in the case of Au NPs/CPIB, the concurrent phase separation occurs simultaneously with hot-electron transfer, making it difficult to discern the behavior of hot electrons. For this reason, pure-halide $CsPbBr_3$ films with and without Au NPs metasurfaces were examined by TAS (**Figure 3a,b**), which can exclude the segregation effect and help determine the hot electron transfer dynamics between perovskite and Au NPs. Figure 3c depicts the normalized transient transmissions ($\Delta T/T$) for both perovskite samples at the peak wavelength, 514 nm, as a function of time following the excitation with an ultrafast light pulse. Due to the generation of photoexcited charge carriers, a sharp increase in transmission over a period of ≈500 fs was first observed for both samples (Region I, photocarrier excitation region). Interestingly, while the transmission of the pure perovskite film rapidly reached saturation, the $\Delta T/T$ of the Au NPs heterostructure counterpart continued to rise over a longer period of 3 ps, confirming the presence of hot electron injection from the Au metasurfaces to the perovskite film (Region II, hot-electron transfer region). The kinetic time constant of hot-electron transfer is further analyzed to be ≈ 550 fs (Figure 3d) and corresponds to the excited state lifetime of the NPs. This finding is consistent with previous studies reporting that hot-electron transfer can occur within a short timescale ranging from tens to several hundred femtoseconds.[43] It should be noted that the obtained kinetics from pure-halide $CsPbBr_3$ might exhibit discrepancies when compared to CPIB, as a result of variations in their bandgap and Fermi levels. Nevertheless, since the hot carriers are endowed with energy much higher than the energy bands of perovskites regardless of their composition, the TAS test can still provide valuable insight into the hot electron injection behaviour at the Au NP/perovskite interfaces.

The metasurface nanostructures offer high tunability, which can be leveraged to control the phase segregation in the mixed-halide perovskite films. We changed the deposition density of Au NPs from 3.8 µg cm^{-2} to 15.2 µg cm^{-2}, and their optical images are shown in **Figure 4a**. The color variation of the metasurfaces implies the changes in the characteristics of plasmonic absorption. The PL spectra of CPIB films with different metasurfaces were monitored under the 532-nm illumination for up to 15 min (Figure 4b), and their peak emission wavelengths over time with 150 s intervals are summarized in Figure 4c. One can see that the phase segregation process of CPIB becomes faster as the Au density increases from 3.8 µg cm^{-2} to 11.4 µg cm^{-2}, while the opposite was observed when the density reaches 15.2 µg cm^{-2}. The largest effect in the 11.4-µg cm^{-2} Au NPs/CPIB sample can be attributed to the density dependence of the plasmonic effect. As shown in the UV-Vis absorption data in Figure 4d, with increasing density, the absorption peak of Au NPs at around 525–535 nm is gradually enhanced, but the absorption peak of the 15.2-µg cm^{-2} Au NPs shifts to ≈560 nm, weakening the plasmonic resonance. Such a density dependence of the absorption wavelength and the hot carrier generation is consistent with the previous reports.[53] The size of Au NPs can also impact the hot-electron coupling. When the NP size decreases, the enhanced quantum effect can promote the hot-electron generation rate, while decreasing the optical absorption due to reduced absorption cross-section. The size-dependent tradeoff between hot-electron generation and optical absorption warrants more research efforts to optimize the hot-electron coupling with perovskite devices for advanced applications.

Since the hot-electron injection in the Au NPs/CPIB system presumably impacts the optoelectronic performance, photocurrent measurements were carried out on samples with interdigitated electrodes (Figure S13, Supporting Information). Figure 4e presents the I-V characteristics of the pristine CPIB and the Au
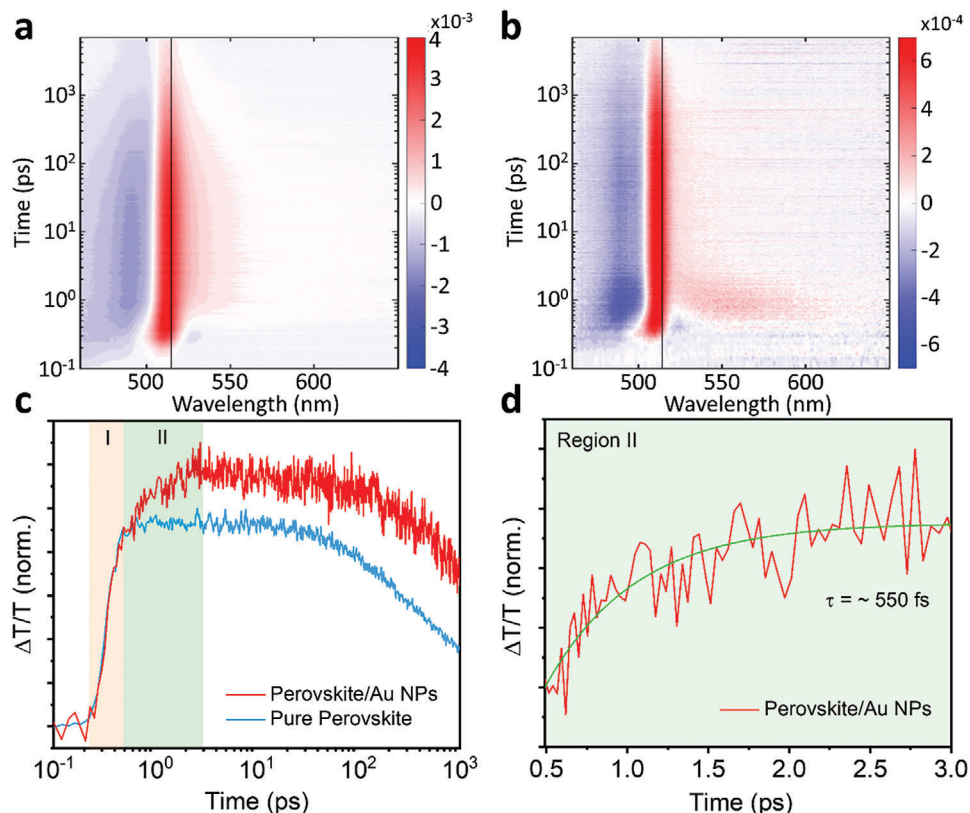
**ADVANCED
SCIENCE NEWS**

www.advancedsciencenews.com

**ADVANCED
FUNCTIONAL
MATERIALS**

www.afm-journal.de

Figure 3. Transient absorption spectroscopy (TAS) measurements to probe the charge carrier dynamics of the perovskite films with and without the Au NPs metasurface structure. 2D plots of $CsPbBr_3$ films a) without and b) with the Au NPs as a function of time and wavelength collected with 450 nm pump with excitation pulse fluence of 6.4 µJ cm^{-2} and 0.05 µJ cm^{-2}. The vertical line (black) denotes the response at 514 nm. c) $\Delta T/T$ trace at 514 nm as a function of time, demonstrating the changes of excited state population over time. After light excitation, the photoexcited charge carriers are generated in the perovskites, leading to a rapid change in transmission for both samples (Region I). With the addition of the Au NPs metasurfaces, the signal change increases over a much longer timeframe (Region II). d) The transfer time constant is determined to be ≈ 550 fs by fitting the hot electron injection region II with an exponential growth function.

NPs/CPIB films, measured in dark and under illumination. The dark current of the pristine CPIB film is at the level of pA, and no significant change in dark current was observed after coating the ultrathin layers of Au NPs. Under light illumination, the photocurrent increased to the level of nA, and the significantly enhanced photocurrent in the Au NPs/CPIB evidenced the effective hot-electron injection from the metasurface nanostructures to the perovskite layer. Note that the photocurrents obtained here correspond to a current density of ≈ 10 mA cm^{-2}, which can substantially impact the phase segregation behavior of mixed-halide perovskites.[54] The time-resolved photoresponse of the Au NPs/CPIB exhibited reversible switching of photocurrent (Figure 4f) as the light was turned on and off. Furthermore, the perovskite film with the Au density of 11.4 µg cm^{-2} revealed the highest photocurrent, confirming the optimal design of the metasurface/perovskite structure as suggested by the simulation results in Figure 1b and c. A lower Au density can diminish the plasmonic effect, while a higher density may reduce the perovskite absorption. The photocurrent data here are in line with the PL result shown in Figure 4b, in which the enhanced free carrier density leads to accelerated PL peak shift. The statistic PL and photocurrent for samples with different Au NPs densities are summarized in Table S1 (Supporting Information). These results also

exclude the role of defects that would suppress the photocurrent, and instead, the hot-electron injection from the Au NP metasurfaces dominates the regulation of the optoelectronic properties of the mixed-halide perovskites.[12,54,55] It is worth noting that the hot electron may provide some level of heating at local positions, especially in the area contacted with Au NPs. However, the partially increased temperatures are unlikely to significantly tune the phase segregation behavior in the entire film according to the reported thermodynamic calculation.[30] Instead, the increased carrier density plays a dominant role in the phase segregation as evidenced by Figure 4c,e. The response time of CPIB photoconductors with and without Au NPs was also measured (Figure S14, Supporting Information). Both devices revealed a similar rise time of around 100 ns, while the fall time decreased from 65 µs to 58 µs after imposing the metasurface, which implies the efficient charge transfer between the CPIB layer and the Au NPs.

Since hot-electron injection plays a key role in the metasurface/perovskite system, electrical gating was introduced to regulate the hot-electron transfer and to tune its impact on perovskite optical properties and phase segregation (**Figure 5a**). Here, both top electrodes are grounded to avoid parasitic horizontal current flow, which would hinder the examination of the hot-electron effect. The pristine CPIB and Au NPs (11.4-µg cm^{-2})/CPIB films
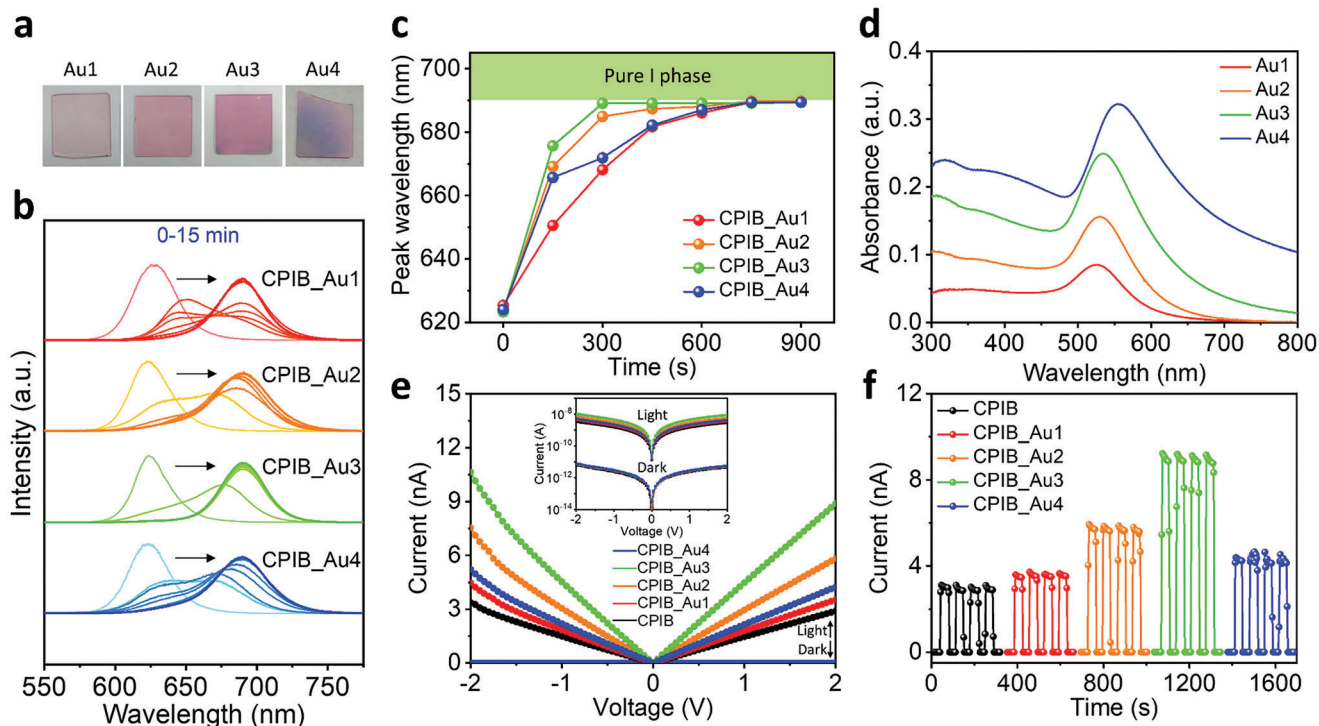
Figure 4. a) Optical images of Au NPs with different deposition densities on transparent glasses to highlight their colors (Au1: 3.8 µg cm^{-2}; Au2: 7.6 µg cm^{-2}; Au3: 11.4 µg cm^{-2}; Au4: 15.2 µg cm^{-2}). b) Time-dependent PL spectra of Au NPs/CPIB films with different Au deposition densities under 532-nm illumination (5 mW cm^{-2}). Arrows illustrate the direction of the time stream up to 15 min with 150 s intervals. c) PL peak positions over time of the Au NPs/CPIB films extracted from Figure 4b. d) UV–vis absorption spectra of Au NPs (on glass substrate) with deposition density from 3.8 µg cm^{-2} to 15.2 µg cm^{-2}. e) I–V characteristics of pristine CPIB and Au NPs/CPIB films with Au density from 3.8 µg cm^{-2} to 15.2 µg cm^{-2} under illumination and in the dark. f) Photoresponse of the pristine CPIB film and different Au NPs/CPIB films measured under a bias of 2 V as the light is switched on and off.
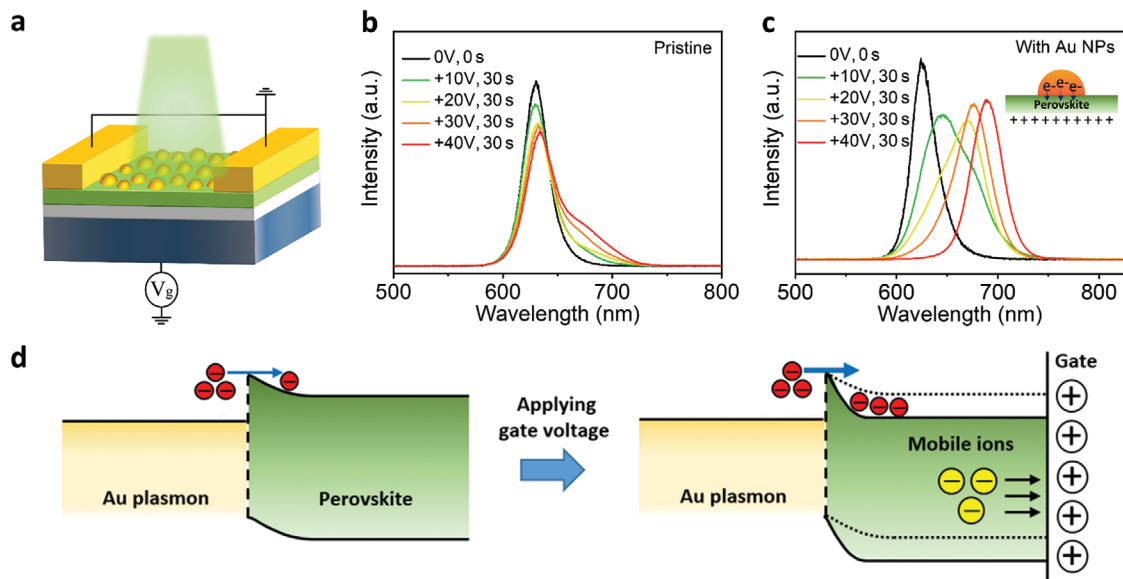

Figure 5. a) Illustration of the experimental setup for controlling the phase segregation and photoluminescence using electrical gating. PL spectra of b) the pristine CPIB film and c) the Au NPs/CPIB heterostructure before and after 532-nm excitation (5 mW cm^{-2}) for 30 s with different gate biases. d) Illustration of Au NPs/CPIB band alignments without and with a gate bias.

2402935 (8 of 13)

were illuminated with a 532-nm laser (5 mW cm^{-2}) and a positive gate voltage bias was applied to the bottom electrode at the same time. The PL spectra of two samples before and after applying the illumination/gate bias are shown in Figure 5b,c. When the gate bias increases from 10 V to 40 V, only a small variation in PL spectra takes place in the pristine CPIB and the peak position of mixed halide emission remains almost unchanged. In addition, the extended band tails indicate that the electrical field does promote the halide ion migration[32,56] but is not enough to trigger the entire phase demixing in our experimental setup. On the other hand, for the Au NPs/CPIB heterostructure, a significant peak shift toward the I-rich emission was observed as the gate voltage increased, indicating a large enhancement of halide segregation. Since electrical gating cannot shift the PL peak to I-rich domain for the pristine counterpart (Figure 5b), the substantially enhanced halide demixing in Au NPs/CPIB (Figure 5c) is mainly attributed to the promoted hot-electron transfer under a stronger positive gate bias. The gate tuning of hot-electron transfer has also been reported previously in other plasmon/semiconductor systems.[57] As illustrated in Figure 5d, when applying a positive gate bias, negative-charged mobile ions and free electrons can move toward the dielectric interface, which acts like n-type doping and enhances the probability of hot-electron transfer across the Schottky junction at the Au/perovskite interface.[57] Consequently, the increased carrier density in the Au NPs/CPIB film under the electrical gating enhances the phase segregation. Noteworthily, to the best of our knowledge, the experiment presented here is the first demonstration of tuning phase segregation of mixed-halide perovskites using a gate bias. The gate-tunable phase segregation of Au NPs/CPIB film not only confirms the important role of hot-electron transfer in the hybrid nanostructures but also provides an additional opportunity to control the mixed-halide phase and photoluminescence in plasmonic perovskite devices. Furthermore, unlike previous approaches entailing the modification of crystal size and defect characteristics during synthesis to change the phase segregation properties of mixed-halide perovskites,[34,35] this study introduces post-synthesis tuning with a gate bias to modulate the hot-electron transfer efficiency, offering unprecedented flexibility to regulate the optical properties of perovskites for versatile applications such as nonlinear ReLU output conversion, as demonstrated in the latter section.

To further confirm the role of hot-electron transfer in our design, a polymethyl methacrylate (PMMA) layer with a thickness of ≈100 nm was spin-coated on perovskite film before the metasurface deposition to form Au NPs/PMMA/CPIB structure, as illustrated in Figure S15a (Supporting Information). The PL spectra of Au NPs/PMMA/CPIB film were measured using the same illumination period and positive gate biasing (Figure S15b, Supporting Information). The PL data indicate that the sample retained the mixed halide emission, and no phase segregation was observed at different gate voltages. In this control sample, the addition of a 100-nm PMMA interlayer would block the hot-electron injection from the metasurface to the CPIB, and therefore, no phase segregation occurred due to much lower carrier density. According to these results, we conclude that the gate-dependent phase segregation of Au NPs/CPIB film in Figure 5c should be attributed to hot-electron transfer across the interface, which can be effectively tuned by using a positive gate bias.[57] Since elec-

trical fields might also facilitate ion migration,[32,56] the negative gate bias conditions (−10, −20, −30, and -40 V) were also tested (Figure S16, Supporting Information). Interestingly, negligible PL peak shifts were observed for the Au NPs/CPIB film, indicating that the electrical field is not the main reason for the phase segregation. The dependence on the bias polarity can be better explained by the hot-electron behavior because the negative bias does not facilitate the hot-electron transfer process, leading to unchanged or even lower carrier density in perovskite film and retaining the mixed-halide phases. Similar observations have also been reported that the hot-electron transfer in the plasmonic heterostructure was enhanced under a positive gate bias while reduced under a negative one.[57,58] To understand the impact of electrical gating in-depth, dark recoveries of Au NPs/CPIB without and with gate bias were performed, respectively, after light-gate synergistically triggered phase demixing (Figure S17, Supporting Information). Compared to the typical phase remixing in dark, it was found that the addition of either positive or negative gates would delay the recovery process, which can be attributed to the enhanced ion accumulation in the presence of electric fields,[37] leading to slower processes of halide remixing.

In this work, the measurements were undertaken based on fresh Au NPs/CPIB samples. To further understand the stability of the Au NPs/CPIB heterostructures, PL and X-ray photoelectron spectroscopy (XPS) analysis were performed on specimens before and after 3 cycles of light-induced phase segregation measurements (at 0 day) and after storing the sample in air for 3 days. As shown in the PL measurements in Figure S18a (Supporting Information), compared to the fresh state, the Au NPs/CPIB retains a high PL emission of ≈93% after reversible phase segregation measurements, indicating its good resistance against the light soaking used in our experiments. Furthermore, no apparent defect peaks were observed on the sample after phase segregation measurements in the XPS spectrum (Figure S18b, Supporting Information) and, together with the enhanced current density and gate tuning observed in Figures 4e,5c, we can conclude that the accelerated phase demixing in the Au NPs/CPIB is due to hot-carrier transfer at the heterostructure interface rather than triggering by defects. However, after storing the sample in air for 3 days (≈50% relative humidity), the light coupling effect of Au NPs/CPIB was drastically decreased (Figure S18a, Supporting Information), and the gate-tunable segregation property was largely lost compared to the fresh sample (Figure S18c, Supporting Information). XPS analysis (Figure S18b, Supporting Information) revealed that undercharged Pb^0 appeared on the aged perovskite surface, which can significantly increase the nonradiative recombination and degrade the optical properties. Due to the ionic nature of perovskite materials, stability is a long-lasting issue in perovskite-related research.[59,60] Under a humid environment, the interfacial reactions between Au and CPIB can be triggered by moisture.[61,62] The interfacial defects would hinder the hot-electron transfer in the heterostructure, thus obscuring the gate-tuning effect in the Au NPs/CPIB. The adverse interfacial reactions can be potentially addressed by sample encapsulation and incorporating a thin interlayer between the metal plasmonic NPs and the perovskite layer.[63] As an example, we adopted a thin PCBM electron transport layer to form an Au NPs/PCBM/CPIB structure, in which the electron transport layer allows the transfer of hot electrons and slows down Au diffusion, if any, into the
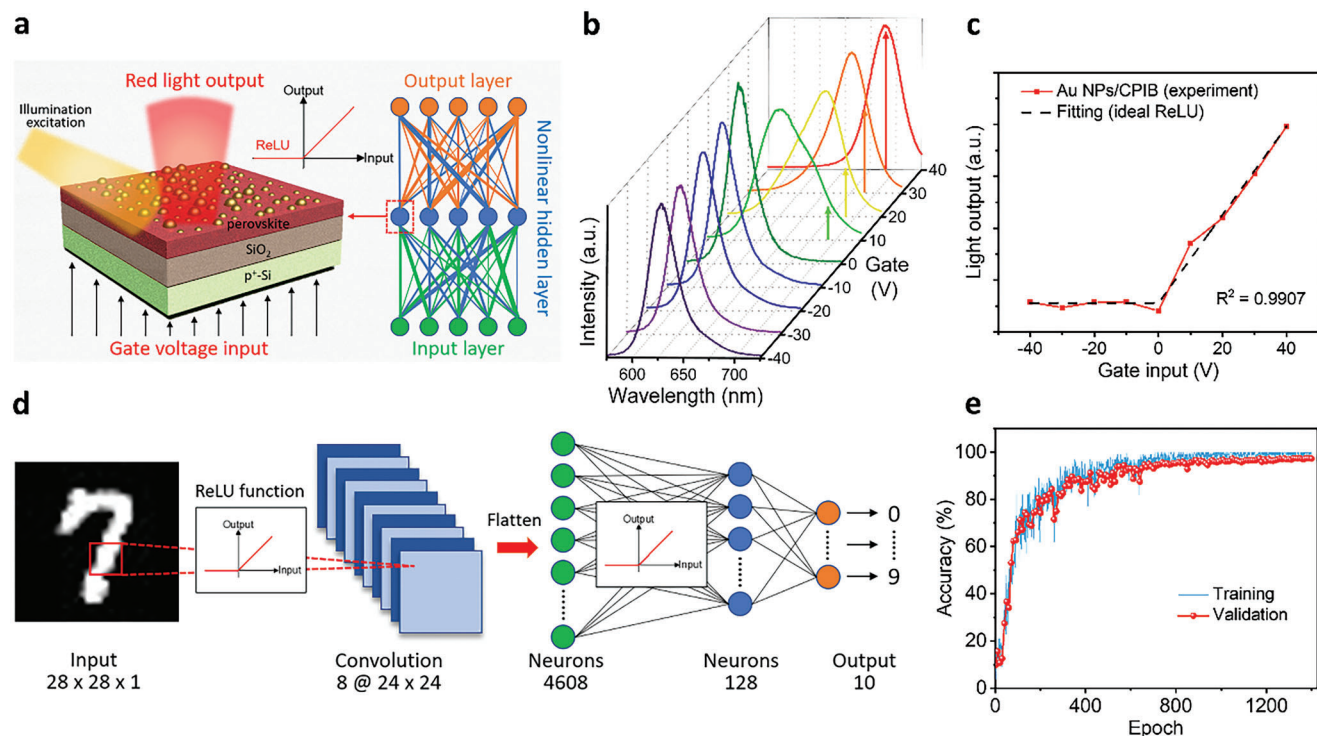
**ADVANCED
SCIENCE NEWS**

www.advancedsciencenews.com

**ADVANCED
FUNCTIONAL
MATERIALS**

www.afm-journal.de

Figure 6. a) Metasurface/perovskite device for presenting the ReLU function in a nonlinear hidden layer to convert gate voltage input to optical output. b) PL optical response characteristic of the metasurface/perovskite device under a series of gate inputs from −40 to 40 V. The light emissions from I-rich domains are highlighted by the arrows. c) Output signal (red light intensity at 685–690 nm) versus input signal (gate voltage) of the metasurface/perovskite converter. d) Architecture of convolution ANN based on electrical-to-optical ReLU. e) Handwritten digit recognition rate as a function of learning processes.

CPIB film at the same time. As shown in Figure S19 (Supporting Information), the modulation of phase segregation was maintained when incorporating the thin PCBM interlayer, which not only provides an additional means towards heterostructure engineering with desired properties but also confirms from another angle that the accelerated phase segregation is not a result of lattice defects induced by Au diffusion.[64–66] Here, the thickness of PCBM is ≈ 20 nm,[67] which can slightly hinder the hot-electron transfer as the segregation in Au NPs/PCBM/CPIB is not as fast as the Au NPs/CPIB counterpart in Figure 2d. Future research efforts are warranted to optimize the interlayer thickness, thereby simultaneously ensuring intact sharp interface and efficient hot-carrier transfer.

As the foundation of artificial intelligence, research on neural networks has achieved impressive progress.[68] However, electronic artificial neural networks (ANNs) are facing inherent bottlenecks, such as the susceptibility to interferences and the correlation between computation speed and energy loss.[69,70] As an alternative, photonic ANNs have been exploited due to their ultra-low power consumption, sub-nanosecond operation speed, and abundant computing parallelism.[70] Despite their tremendous success in linear computation, photonic ANN models are difficult to execute nonlinear functions because of their limited and invariable network complexity compared to electronic circuits.[71] Recently, in order to combine the advantages of electronic and photonic ANNs for high-performance and energy-efficient neuromorphic computing, researchers have turned their attention

to exploring optoelectronic networks with a focus on electrical-to-optical and optical-to-electrical converters, which play a key role in connecting the neural networks.[69,72,73] In a representative work, Xu et al. developed a linear optical-to-electrical converter using an opto-resistive switching device in electronic-photonic ANNs and realized intricate functional computation.[69]

As demonstrated above, the optical properties of metasurface/perovskite architecture can be systematically tuned through electrical gating, which offers a new platform for developing electrical-to-optical converters in ANN hidden layers (**Figure 6a**). In this metasurface/perovskite converter, the gate voltage represents the electrical input while the PL emission of iodine-rich domains (wavelengths from 685 nm to 690 nm) is read as the optical output. The gate-dependent optical spectra of the metasurface/perovskite device are shown in Figure 6b, in which the iodine-domain emission is generally inhibited with gate biases from -40 V to 0 V while linearly enhanced from 0 V 40 V. This characteristic superbly matches the ReLU function, which is the most extensively used nonlinear activation function in ANN deep learning. The relationship between electrical input and optical output of the metasurface/perovskite device is plotted in Figure 6c, which can be perfectly fitted by the ReLU function, defined as $ReLU(x) = \max(0, ax) + b$, where a and b are constants, x is electrical input, and $ReLU(x)$ represents the optical output. As a result, a high coefficient of determination (R^2) of 0.9907 is obtained, suggesting that the metasurface/perovskite devices can be ideal electrical-to-optical converters to perform

nonlinear activation ReLU function. Different from recently developed electrical- and optical-only ReLU converters (Table S2, Supporting Information), the electrical-to-optical ReLU converter has not been achieved thus far, which possesses great potential for future network connections in electronic-photonic ANNs.

We further adopted the experimental obtained electrical-to-optical ReLU in an ANN application to classify handwritten digits from the MNIST database. The convolution ANN structure is shown in Figure 6d. For the given classification challenge, we set the batch size to 100 and the learning rate at 0.001, using a 3×3 kernel size and a stride of 1 for the convolution. With the electrical-to-optical ReLU function implemented in the ANN (Figure 6e), a high accuracy rate of 97.4% was achieved, a figure in line with what was attained when employing the ideal ReLU and other nonlinear functions for the identical neural network (Table S3, Supporting Information). This outcome underscores the validity and potential of electrical-to-optical ReLU as a nonlinear activation function in ANN applications.

3. Conclusion

In summary, we incorporated the hot-electron injection into the perovskite optoelectronics by constructing Au NPs metasurfaces and studied its impact on photoluminescence and phase segregation of CPIB films. Owing to efficient hot-electron coupling with the plasmonic Au NPs, the photocurrent and the light-induced phase segregation of CPIB were substantially enhanced. Furthermore, a gate electric field was used to tune the hot-electron injection, thereby achieving fine control of photoluminescence and phase segregation in the CPIB films. Due to the capability of near-field light-harvesting of the metasurface, we realized control of perovskite phases at localized positions by selectively patterning the plasmonic metasurfaces on the perovskite film. Finally, we demonstrated that the superior property tunability of metasurface/perovskite heterostructure provides a potential solution for electrical-to-optical converters to perform nonlinear activation ReLU functions in ANN hidden layers. With suitable metasurface management strategies, the functionality and viability of mixed-halide perovskites in a wide range of applications can be rationally engineered on demand. This study opened a new door toward leveraging light and hot-carrier management techniques to propel the development of mixed-halide perovskite devices. Additionally, the plasmonic metasurfaces presented here demonstrate desirable capabilities to enhance PL emission and photocarrier density, which is promising to be further leveraged to advance perovskite optoelectronics. Besides the optimization of hot-electron injection, light absorption of perovskite films can be further optimized in future by careful design of the metasurface and perovskite layers. Finally, such rationally designed perovskite/metasurface heterostructures may be applied in other areas including photovoltaic, photodetection and photocatalysis to promote the perovskite-based technologies.

4. Experimental Section

Fabrication of Perovskite Thin Films and Au NP Metasurfaces: The CPIB nanocrystals were synthesized employing a hot-injection method, followed by purification and redispersion processes, as reported in the previous work.[41] The SiO$_2$/Si substrates were cleaned by ultrasonication in acetone (20 min), ethanol (10 min) and deionised water (10 min), and then cleaned by O$_2$ plasma at a power of 75 W for 2 min. The CPIB nanocrystals were spin-coated onto the SiO$_2$/Si substrate at 3000 rpm for 1 min. Then, methyl acetate was dropped onto the film for soft soaking. After 1 min soaking, the methyl acetate was removed by spinning at 3000 rpm. The perovskite film was annealed at 120 °C for 10 min. All the processes were performed in a glove box with inert atmosphere. To construct the Au NP metasurfaces, different densities of Au were thermal evaporated on the CPIB films with a slow deposition rate of 0.019 µg s^{-1} cm^{-2}. Finally, the Au NP/CPIB samples were rapidly annealed at 120 °C for 3 min in a glove box. For the experiments using an electron transport interlayer, PCBM/chlorobenzene (15 mg mL^{-1}) solution was spin-coated onto the perovskite films at 4500 rpm for 30 s in a glove box.

Optical and Device Measurements: Fresh Au/CPIB samples (0 day) were used for all measurements to avoid degradation, except for the stability test. The CPIB nanocrystals were examined using transmission electron microscopy (model JEM-F200, JEOL Ltd.) operated at 200 kV. X-ray diffraction measurement on CPIB was undertaken by a Bruker D8 ADVANCE diffractometer. The surface morphologies of pristine and Au NPs/CPIB films were studied by a high-resolutionSEM (model Nova NanoSEM 450, FEI) with a voltage setting of 5 kV. The absorption spectra of different samples were measured using a double-beam UV/Vis/NIR spectrophotometer (model Lambda 1050, PerkinElmer). WITec Alpha300 confocal spectroscopy equipped with a 532-nm laser was employed for PL measurements and investigation of phase segregation in mixed-halide perovskite films with an intensity of 5 mW cm^{-2} ($\approx$1.34 $\times$ 10^{16} photons cm^{-2} s^{-1}). For PL measurements with a gate field, a commercial field-effect transistor measurement adapter (Fraunhofer-Gesellschaft) was used to apply the gate bias. The dynamics of hot-electron injection were examined using the HELIOS transient absorption spectrometer, driven by a cavity-dumped Ti: Sapphire laser operating at 800 nm with an output train of $\approx$80 fs pulses. Within the 4 W of total output power, a dedicated 80 mW was allocated for probe supercontinuum generation. The remaining power was directed to a TOPAS Optical Parametric Amplifier to produce the pump wavelengths essential for this investigation. The measurements were performed using magic angle transient absorption spectroscopy with an excitation wavelength of 450 nm and a white light continuum probe. Time-resolved PL measurements were carried out using a confocal fluorescence microscope (MicroTime 200, PicoQuant) and a 470-nm excitation laser combined with a 519-nm long-pass filter for PL intensity monitoring. The laser spot size was around 2 µm and the collecting time was set to 100 s. XPS analysis was performed using an Escalab MkII system equipped with monochromatized Al Kα radiation under a pressure of 5.0 $\times$ 10^{-7} Pa. A Keithley 4200-SCS semiconductor characterization system was used to measure the I-V characteristics of perovskite devices.

Supporting Information

Supporting Information is available from the Wiley Online Library or from the author.

Conflict of Interest

The authors declare no conflict of interest.

Data Availability Statement

The data that support the findings of this study are available from the corresponding author upon reasonable request.

Keywords

hot electron, mixed-halide perovskite, phase segregation, photoluminescence, plasmonics

[1] Y. Wang, X. M. Li, J. Z. Song, L. Xiao, H. B. Zeng, H. D. Sun, *Adv. Mater.* **2015**, *27*, 7101.

[2] M. V. Kovalenko, L. Protesescu, M. I. Bodnarchuk, *Science* **2017**, *358*, 745.

[3] X. L. Zhang, H. Liu, W. G. Wang, J. B. Zhang, B. Xu, K. L. Karen, Y. J. Zheng, S. Liu, S. M. Chen, K. Wang, X. W. Sun, *Adv. Mater.* **2017**, *29*, 1606405.

[4] P. R. Anandan, M. Nadeem, C.-H. Lin, S. Singh, X. Guan, J. Kim, S. Shahrokhi, M. Z. Rahaman, X. Geng, J.-K. Huang, H. Nguyen, H. Hu, P. Sharma, J. Seidel, X. Wang, T. Wu, *Appl. Phys. Rev.* **2023**, *10*, 041312.

[5] C.-Y. Huang, H. Li, Y. Wu, C.-H. Lin, X. Guan, L. Hu, J. Kim, X. Zhu, H. Zeng, T. Wu, *Nano-Micro Lett.* **2022**, *15*, 16.

[6] M. T. Vijjapu, M. E. Fouda, A. Agambayev, C. H. Kang, C.-H. Lin, B. S. Ooi, J.-H. He, A. M. Eltawil, K. N. Salama, *Light Sci. Appl.* **2022**, *11*, 3.

[7] Best Research-Cell Efciency Chart, https://www.nrel.gov/pv/assets/pdfs/best-research-cell-efficiencies.pdf (accessed: February 2024).

[8] X. Guan, Z. Lei, X. Yu, C.-H. Lin, J.-K. Huang, C.-Y. Huang, L. Hu, F. Li, A. Vinu, J. Yi, T. Wu, *Small* **2022**, *18*, 2203311.

[9] Q. A. Akkerman, G. Raino, M. V. Kovalenko, L. Manna, *Nat. Mater.* **2018**, *17*, 394.

[10] J. Shamsi, A. S. Urban, M. Imran, L. De Trizio, L. Manna, *Chem. Rev.* **2019**, *119*, 3296.

[11] X. Guan, T. Wan, L. Hu, C.-H. Lin, J. Yang, J.-K. Huang, C.-Y. Huang, S. Shahrokhi, A. Younis, K. Ramadass, K. Liu, A. Vinu, J. Yi, D. Chu, T. Wu, *Adv. Funct. Mater.* **2022**, *32*, 2110975.

[12] A. J. Knight, L. M. Herz, *Energy Environ. Sci.* **2020**, *13*, 2024.

[13] H. F. Zarick, N. Soetan, W. R. Erwin, R. Bardhan, *J. Mater. Chem. A* **2018**, *6*, 5507.

[14] C. Clavero, *Nat. Photonics* **2014**, *8*, 95.

[15] M. L. Brongersma, N. J. Halas, P. Nordlander, *Nat. Nanotechnol.* **2015**, *10*, 25.

[16] S. Linic, U. Aslam, C. Boerigter, M. Morabito, *Nat. Mater.* **2015**, *14*, 567.

[17] U. Aslam, V. G. Rao, S. Chavez, S. Linic, *Nat. Catal.* **2018**, *1*, 656.

[18] E. Cortés, L. V. Besteiro, A. Alabastri, A. Baldi, G. Tagliabue, A. Demetriadou, P. Narang, *ACS Nano* **2020**, *14*, 16202.

[19] S. Linic, S. Chavez, R. Elias, *Nat. Mater.* **2021**, *20*, 916.

[20] X. Y. Huang, H. B. Li, C. F. Zhang, S. J. Tan, Z. Z. Chen, L. Chen, Z. D. Lu, X. Y. Wang, M. Xiao, *Nat. Commun.* **2019**, *10*, 1163.

[21] Y. H. Dong, Y. Gu, Y. S. Zou, J. Z. Song, L. M. Xu, J. H. Li, F. Xue, X. M. Li, H. B. Zeng, *Small* **2016**, *12*, 5622.

[22] R. S. Moakhar, S. Gholipour, S. Masudy-Panah, A. Seza, A. Mehdikhani, N. Riahi-Noori, S. Tafazoli, N. Timasi, Y. F. Lim, M. Saliba, *Adv. Sci.* **2020**, *7*, 1902448.

[23] C. Ma, C. X. Liu, J. F. Huang, Y. H. Ma, Z. X. Liu, L. J. Li, T. D. Anthopoulos, Y. Han, A. Fratalocchi, T. Wu, *Sol. RRL* **2019**, *3*, 1900138.

[24] S. J. Yoon, S. Draguta, J. S. Manser, O. Sharia, W. F. Schneider, M. Kuno, P. V. Kamat, *ACS Energy Lett.* **2016**, *1*, 290.

[25] X. Tang, M. van den Berg, E. Gu, A. Horneber, G. J. Matt, A. Osvet, A. J. Meixner, D. Zhang, C. J. Brabec, *Nano Lett.* **2018**, *18*, 2172.

[26] W. Mao, C. R. Hall, A. S. R. Chesman, C. Forsyth, Y.-B. Cheng, N. W. Duffy, T. A. Smith, U. Bach, *Angew. Chem., Int. Ed.* **2019**, *58*, 2893.

[27] Y. T. Wang, X. Quintana, J. Y. Kim, X. W. Guan, L. Hu, C. H. Lin, B. T. Jones, W. J. Chen, X. M. Wen, H. W. Gao, T. Wu, *Photonics Res* **2020**, *8*, A56.

[28] A. Zanetta, Z. Andaji-Garmaroudi, V. Pirota, G. Pica, F. U. Kosasih, L. Gouda, K. Frohna, C. Ducati, F. Doria, S. D. Stranks, G. Grancini, *Adv. Mater.* **2022**, *34*, 2105942.

[29] R. Li, B. Chen, N. Ren, P. Wang, B. Shi, Q. Xu, H. Zhao, W. Han, Z. Zhu, J. Liu, Q. Huang, D. Zhang, Y. Zhao, X. Zhang, *Adv. Mater.* **2022**, *34*, 2201451.

[30] F. Brivio, C. Caetano, A. Walsh, *J. Phys. Chem. Lett.* **2016**, *7*, 1083.

[31] Y. T. Wang, X. W. Guan, W. J. Chen, J. Yang, L. Hu, J. Yang, S. Li, K. Kalantar-Zadeh, X. M. Wen, T. Wu, *ACS Appl. Mater. Interfaces* **2020**, *12*, 38376.

[32] H. C. Zhang, X. Fu, Y. Tang, H. Wang, C. F. Zhang, W. W. Yu, X. Y. Wang, Y. Zhang, M. Xiao, *Nat. Commun.* **2019**, *10*, 1088.

[33] S. Draguta, O. Sharia, S. J. Yoon, M. C. Brennan, Y. V. Morozov, J. M. Manser, P. V. Kamat, W. F. Schneider, M. Kuno, *Nat. Commun.* **2017**, *8*, 200.

[34] A. F. Gualdron-Reyes, S. J. Yoon, E. M. Barea, S. Agouram, V. Munoz-Sanjose, A. M. Melendez, M. E. Nino-Gomez, I. Mora-Sero, *ACS Energy Lett.* **2019**, *4*, 54.

[35] L. Hu, X. Guan, W. Chen, Y. Yao, T. Wan, C.-H. Lin, N. D. Pham, L. Yuan, X. Geng, C.-Y. Huang, S. Cheong, R. D. Tilley, X. Wen, D. Chu, S. Huang, T. Wu, *ACS Energy Lett.* **2021**, *6*, 1649.

[36] P. Caprioglio, S. Caicedo-Dávila, T. C.-J. Yang, C. M. Wolff, F. Peña-Camargo, P. Fiala, B. Rech, C. Ballif, D. Abou-Ras, M. Stolterfoht, S. Albrecht, Q. Jeangros, D. Neher, *ACS Energy Lett.* **2021**, *6*, 419.

[37] S. G. Motti, J. B. Patel, R. D. J. Oliver, H. J. Snaith, M. B. Johnston, L. M. Herz, *Nat. Commun.* **2021**, *12*, 6955.

[38] P. Mao, C. Liu, F. Song, M. Han, S. A. Maier, S. Zhang, *Nat. Commun.* **2020**, *11*, 1538.

[39] S. Zaman, M. Hossain, *OSA Contin.* **2020**, *3*, 3082.

[40] M. Moskovits, *Nat. Nanotechnol.* **2015**, *10*, 6.

[41] J. Kim, L. Hu, H. J. Chen, X. W. Guan, P. R. Anandan, F. Li, J. B. Tang, C. H. Lin, K. Kalantar-Zadeh, A. Tricoli, T. Wu, *ACS Mater. Lett.* **2020**, *2*, 1368.

[42] V. G. Kravets, A. V. Kabashin, W. L. Barnes, A. N. Grigorenko, *Chem. Rev.* **2018**, *118*, 5912.

[43] A. Furube, S. Hashimoto, *NPG Asia Mater* **2017**, *9*, e454.

[44] A. Younis, C.-H. Lin, X. Guan, S. Shahrokhi, C.-Y. Huang, Y. Wang, T. He, S. Singh, L. Hu, J. R. D. Retamal, J.-H. He, T. Wu, *Adv. Mater.* **2021**, *33*, 2005000.

[45] C. Zhou, T. Zhang, C. Zhang, X. Liu, J. Wang, J. Lin, X. Chen, *Adv. Sci.* **2022**, *9*, 2103491.

[46] J. Cui, C. Chen, J. Han, K. Cao, W. Zhang, Y. Shen, M. Wang, *Adv. Sci.* **2016**, *3*, 1500312.

[47] W. Zhang, M. Saliba, S. D. Stranks, Y. Sun, X. Shi, U. Wiesner, H. J. Snaith, *Nano Lett.* **2013**, *13*, 4505.

[48] H. Kim, R. M. Kim, S. D. Namgung, N. H. Cho, J. B. Son, K. Bang, M. Choi, S. K. Kim, K. T. Nam, J. W. Lee, J. H. Oh, *Adv. Sci.* **2022**, *9*, 2104598.

[49] X. Wang, Y. C. Ling, X. J. Lian, Y. Xin, K. B. Dhungana, F. Perez-Orive, J. Knox, Z. Z. Chen, Y. Zhou, D. Beery, K. Hanson, J. Shi, S. C. Lin, H. W. Gao, *Nat. Commun.* **2019**, *10*, 695.

[50] S. K. Gautam, M. Kim, D. R. Miquita, J.-E. Bourée, B. Geffroy, O. Plantevin, *Adv. Funct. Mater.* **2020**, *30*, 2002622.

[51] Y. C. Chen, Y. S. Huang, H. Huang, P. J. Su, T. P. Perng, L. J. Chen, *Nano Energy* **2020**, *67*, 104225.

[52] C. X. Zhang, Q. Luo, J. H. Shi, L. Y. Yue, Z. B. Wang, X. H. Chen, S. M. Huang, *Nanoscale* **2017**, *9*, 2852.

[53] V. N. Rai, A. K. Srivastava, C. Mukherjee, S. K. Deb, *Appl. Opt.* **2012**, *51*, 2606.

[54] I. L. Braly, R. J. Stoddard, A. Rajagopal, A. R. Uhl, J. K. Katahara, A. K. Y. Jen, H. W. Hillhouse, *ACS Energy Lett.* **2017**, *2*, 1841.

[55] T. Duong, H. K. Mulmudi, Y. L. Wu, X. Fu, H. P. Shen, J. Peng, N. D. Wu, H. T. Nguyen, D. Macdonald, M. Lockrey, T. P. White, K. Weber, K. Catchpole, *ACS Appl. Mater. Interfaces* **2017**, *9*, 26859.

[56] A. J. Knight, J. B. Patel, H. J. Snaith, M. B. Johnston, L. M. Herz, *Adv. Energy Mater.* **2020**, *10*, 1903488.

[57] H.-Y. Lan, Y.-H. Hsieh, Z.-Y. Chiao, D. Jariwala, M.-H. Shih, T.-J. Yen, O. Hess, Y.-J. Lu, *Nano Lett.* **2021**, *21*, 3083.

[58] H. Shokri Kojori, J.-H. Yun, Y. Paik, J. Kim, W. A. Anderson, S. J. Kim, *Nano Lett.* **2016**, *16*, 250.

[59] C.-H. Lin, B. Cheng, T.-Y. Li, J. R. D. Retamal, T.-C. Wei, H.-C. Fu, X. Fang, J.-H. He, *ACS Nano* **2019**, *13*, 1168.

[60] S. Shahrokhi, M. Dubajic, Z.-Z. Dai, S. Bhattacharyya, R. A. Mole, K. C. Rule, M. Bhadbhade, R. Tian, N. Mussakhanuly, X. Guan, Y. Yin, M. P. Nielsen, L. Hu, C.-H. Lin, S. L. Y. Chang, D. Wang, I. V. Kabakova, G. Conibeer, S. Bremner, X.-G. Li, C. Cazorla, T. Wu, *Small* **2022**, *18*, 2200847.

[61] L. Zhao, R. A. Kerner, Z. Xiao, Y. L. Lin, K. M. Lee, J. Schwartz, B. P. Rand, *ACS Energy Lett.* **2016**, *1*, 595.

[62] J. Kim, A. T. John, H. Li, C.-Y. Huang, Y. Chi, P. R. Anandan, K. Murugappan, J. Tang, C.-H. Lin, L. Hu, K. Kalantar-Zadeh, D. Chu, T. Wu, *Small Methods* **2023**, *7*, 2300417.

[63] C.-H. Lin, L. Hu, X. Guan, J. Kim, C.-Y. Huang, J.-K. Huang, S. Singh, T. Wu, *Adv. Mater.* **2022**, *34*, 2108616.

[64] K. Domanski, J.-P. Correa-Baena, N. Mine, M. K. Nazeeruddin, A. Abate, M. Saliba, W. Tress, A. Hagfeldt, M. Grätzel, *ACS Nano* **2016**, *10*, 6306.

[65] S. J. Yoon, M. Kuno, P. V. Kamat, *ACS Energy Lett.* **2017**, *2*, 1507.

[66] A. J. Barker, A. Sadhanala, F. Deschler, M. Gandini, S. P. Senanayak, P. M. Pearce, E. Mosconi, A. J. Pearson, Y. Wu, A. R. Srimath Kandada, T. Leijtens, F. De Angelis, S. E. Dutton, A. Petrozza, R. H. Friend, *ACS Energy Lett.* **2017**, *2*, 1416.

[67] K. Elkhouly, I. Goldberg, H.-G. Boyen, A. Franquet, V. Spampinato, T.-H. Ke, R. Gehlhaar, J. Genoe, J. Hofkens, P. Heremans, W. Qiu, *Adv. Opt. Mater.* **2021**, *9*, 2100586.

[68] F. Chen, S. Zhang, L. Hu, J. Fan, C.-H. Lin, P. Guan, Y. Zhou, T. Wan, S. Peng, C.-H. Wang, L. Wu, T. M. Furlong, N. Valanoor, D. Chu, *Adv. Funct. Mater.* **2023**, *33*, 2300266.

[69] Z. Xu, B. Tang, X. Zhang, J. F. Leong, J. Pan, S. Hooda, E. Zamburg, A. V.-Y. Thean, *Light Sci. Appl.* **2022**, *11*, 288.

[70] W. Ma, Z. Liu, Z. A. Kudyshev, A. Boltasseva, W. Cai, Y. Liu, *Nat. Photonics* **2021**, *15*, 77.

[71] J. Liu, Q. Wu, X. Sui, Q. Chen, G. Gu, L. Wang, S. Li, *PhotoniX* **2021**, *2*, 5.

[72] Z. Ying, C. Feng, Z. Zhao, S. Dhar, H. Dalir, J. Gu, Y. Cheng, R. Soref, D. Z. Pan, R. T. Chen, *Nat. Commun.* **2020**, *11*, 2154.

[73] B. J. Shastri, A. N. Tait, T. Ferreira de Lima, W. H. P. Pernice, H. Bhaskaran, C. D. Wright, P. R. Prucnal, *Nat. Photonics* **2021**, *15*, 102.

2402935 (13 of 13)